THE JOURNAL OF PHYSICAL CHEMISTRY C

Article

pubs.acs.org/JPCC

Passivation of Nickel Vacancy Defects in Nickel Oxide Solar Cells by Targeted Atomic Deposition of Boron

Cory J. Flynn,[†] Shannon M. McCullough,[†] Lesheng Li,[†] Carrie L. Donley,[‡] Yosuke Kanai,[†] and James F. Cahoon*[,†]

[†]Department of Chemistry, University of North Carolina at Chapel Hill, Chapel Hill, North Carolina 27599-3290, United States

[‡]Chapel Hill Analytical and Nanofabrication Laboratory (CHANL), Department of Applied Physical Sciences, University of North Carolina at Chapel Hill, Chapel Hill, North Carolina 27599-3216, United States

Supporting Information

ABSTRACT: Localized trap states, which are deleterious to the performance of many solar-energy materials, often originate from the under-coordinated bonding associated with defects. Recently, the concept of targeted atomic deposition (TAD) was introduced as a process that permits the passivation of trap states using a vapor-phase precursor that selectively reacts with only the surface defect sites. Here, we demonstrate the passivation of nickel oxide (NiO) with the TAD process using diborane gas for selective, low-temperature deposition of boron (B) under continuous flow in a chemical vapor deposition (CVD) system. NiO is a ubiquitous cathode material used in dye-sensitized solar cells (DSSCs), organic photovoltaic devices, and organo-lead halide perovskite solar cells. The deposition of B at 100 °C is shown to follow first-order kinetics, exhibiting saturation at a B to Ni atomic ratio of ∼10%. Electrochemical measurements, combined with first-principles calculations, indicate that B passivates Ni vacancy defects by partially saturating the bonding of the oxygen atoms adjacent to the vacancy. p-Type DSSCs were fabricated using TAD-treated NiO and show a modest improvement in photovoltaic performance metrics. The results highlight the potential ubiquity of TAD passivation with a range of atomic precursors and vapor-phase processes.

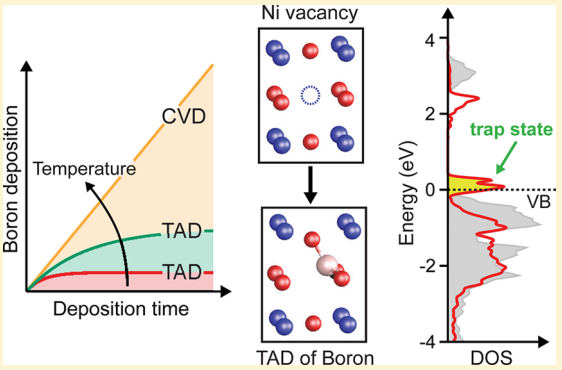

1. INTRODUCTION

With the growth of global energy demand and rise in atmospheric CO_2 levels,[1] carbon-neutral energy sources must continue to be developed and implemented at a rapid pace. Although solar energy conversion using photovoltaic devices has long been sought as a solution,[2] a fundamental problem remains: the diurnal cycle of the Earth prevents continuous power generation. Excess power generated during the day must be stored, ideally in chemical bonds.[3] The tandem dye-sensitized photoelectrosynthetic cell (DSPEC) offers a potential solution by using solar energy to create solar fuels by performing simultaneous water oxidation and CO_2 reduction, mimicking photosynthesis.[4−9] The reduced-carbon products are then stored and combusted as needed. Rather than a single highly efficient electrode, a tandem device is required to increase efficiency[10] and to produce a sufficiently large photopotential to perform both redox reactions.[11,12]

Recent work on optimizing the photoanode of the tandem DSPEC has shown remarkable progress through the utilization of staggered band alignments (e.g., SnO_2/TiO_2),[5,13] chromophore-catalyst assemblies prepared by atomic layer deposition (ALD),[14] and chromophore-catalyst stabilization by ALD overlayers.[5] Work on the photocathode, however, lags behind. To date, much of the work on the photocathode has focused on improving the chromophore by synthesizing donor-π-acceptor molecules,[15−18] creating a hydrophobic layer of protection in the molecules,[19] and improving the light absorption properties.[20]

Although many wide-band-gap p-type semiconductors have been explored as cathode materials (e.g., nickel oxide,[17,18,21−29] spinel cobalt oxides,[30,31] copper oxides,[32] copper-based delafossites,[33−37] bismuth oxyhalides[38]), NiO remains the champion material in dye-sensitized applications.[21] The still relatively low performance of NiO devices has been attributed to a myriad of issues, including fast surface-mediated recombination, a high dark saturation current density (J_0), black coloring, short hole lifetime, low hole mobility, high series resistance, and low dielectric constant.[39,40] Previous work to improve or mitigate these characteristics has included doping with cobalt,[41] lithium,[42] and magnesium;[24] ALD overlayers of alumina;[27] solution-phase deposition of alumina;[43] increased hole mobility through nanoparticle morphology;[29] and reduced recombination through higher crystallinity.[22,23,44] However, performance is still generally low, and defect sites still limit the device performance.

Received: June 30, 2016

DOI: 10.1021/acs.jpcc.6b06593
J. Phys. Chem. C XXXX, XXX, XXX−XXX

The remarkably large surface trap state density of NiO originates from under-coordinated oxygen atoms adjacent to Ni vacancies in the lattice.[45] We recently demonstrated that these trap states are responsible for the black coloring of the electrodes, short hole lifetime, and high dark saturation current density.[45] Historically, the black coloring in NiO has been attributed to intervalence charge transfer (e.g., $Ni^{2+}-Ni^{3+}$ and $Ni^{3+}-Ni^{4+}$ transitions).[46] However, recent first-principles calculations[45] have shown that the trap states that give rise to the optical transitions are predominately oxygen-based orbitals.

In order to selectively passivate these under-coordinated oxygen atoms, a new process termed targeted atomic deposition (TAD) was recently developed.[45] TAD is a vapor-phase process in which a highly reactive vapor-phase precursor selectively reacts with surface defect sites. In the initial report of the TAD process, trimethyl aluminum was used to passivate defect sites in NiO by the deposition of Al, resulting in the optical and electronic bleaching of the films, an increase in hole lifetimes and decrease in J_0 by more than 10-fold, an increase in the V_{OC} to the theoretical maximum, and a nearly 3-fold increase in photoconversion efficiency.[45] The TAD of Al was performed in a conventional ALD system using deposition temperatures too low for a conventional ALD process. However, the TAD process is amenable to both ALD and chemical vapor deposition (CVD) processes if the deposition conditions can be altered to favor a kinetic and thermodynamic regime that eliminates layered deposition in favor of selective reactions with defect sites. Here, we demonstrate the TAD process in a conventional CVD system with the precursor diborane (B_2H_6), which selectively deposits B at defect sites.

2. MATERIALS AND METHODS

NiO Paste Preparation. A NiO paste was prepared by mixing commercially available spherical nanoparticles (Inframat Advanced Materials) of NiO (16 g), α-terpineol (64.9 g), ethanol (63.1 g), and ethyl cellulose (a 45 g, 10 wt % in ethanol, 5−15 mPa·s solution was combined with a 35 g, 10 wt % in ethanol, 30−50 mPa·s solution). The paste was homogenized by horn sonication, mechanical dispersing, and ball-milling.[47] Mild sonication for 5 min was performed on the day of use.

NiO Film Preparation. A mesoporous layer of NiO (~1 μm in thickness) was deposited onto fluorine-doped tin oxide (FTO; Hartford Glass, TEC15) substrates by spin-casting (Laurell WS-650MZ-23NPP; 5 s at 500 rpm, 30 s at 1500 rpm) and annealing in air (450 °C, 40 min, humidity <20%). The active area was then defined by mechanically removing excess material to form 7.5 × 7.5 mm squares. The electrodes areas were 0.55 ± 0.05 cm^2. B deposition was performed in a home-built CVD system[48] with a 1-in. diameter quartz tube, Lindberg Blue M single-zone furnace, a base pressure of ~3×10^{-3} Torr, and diborane gas (100 ppm in hydrogen; Voltaix). All samples were thermally equilibrated at the deposition temperature of 50, 100, or 150 °C for 5 min before being exposed to diborane at 30 mTorr for 30, 100, 300, or 1000 s using a gas flow rate of 20.0 standard cubic centimeters per minute (sccm). All samples were utilized as-deposited without further annealing.

Solar-Cell Fabrication. The electrode films were immersed in P1 solution (0.1 mM in acetonitrile) overnight, rinsed with acetonitrile, and dried with N_2. Pt counter electrodes were fabricated by sandblasting a hole into Kapton-protected FTO glass. Platinization was performed by thermal decomposition (380 °C, 30 min, humidity <20%) of chloroplatinic acid (5 mM in 2-propanol). A small, 25-μm-thick Surlyn gasket (inner diameter 10 × 10 mm, outer diameter 12 × 12 mm) was utilized to sandwich the working electrode with the platinized counter electrode in a custom-made heat press (150 °C; 10 s). The hole was sealed with Surlyn (150 °C, 5 s) with a polyimide film to prevent adhesion of the Surlyn to the heat press. Z960-like electrolyte [1.0 M 1,3-dimethylimidazolium iodide, iodide (0.03 M), *tert*-butylpyridine (0.5 M), and guanidium thiocynanate (0.1 M) in 85/15 (v/v) acetonitrile/valeronitrile] was vacuum backfilled with a home-built vacuum apparatus. The cell was then sealed (150 °C, 5 s) with a Surlyn film, a microscope coverslip, and a polyimide film. For the average photovoltaic device metrics provided in Table 1, all devices were fabricated and measured on the same day, with the same NiO paste, under identical fabrication and characterization conditions. Average values and standard deviations reflect measurements from four devices.

Characterization. Optical absorption measurements were performed on an Agilent Cary 5000 spectrometer with integrating sphere attachment. Light-harvesting efficiencies (LHE) were calculated by multiplying the absorptance, $(1 - 10^{-A_{total}}) \times 100\% = (100 - \%T)$, of the dyed-loaded NiO films with the fraction of light absorbed by the P1 chromophore, $[A_{P1}/A_{total}]$, where A_{P1} is the absorbance of P1 on the surface of NiO and A_{total} is the total absorbance of the dye-loaded film with $A_{total} = A_{P1} + A_{NiO}$, and A_{NiO} is the absorbance of the NiO film without dye. The LHE values presented here thus are corrected for the background absorbance of the NiO films. Elemental quantification was performed by X-ray photoelectron spectroscopy (XPS) with a Kratos Axis Ultra DLD spectrometer. All XPS data were corrected to the C 1s peak (284.6 eV) and background-corrected. Due to varying experimental intensities, the B-content is reported as the ratio of the B/Ni atomic percent. XPS spectra were fit with Voigt functions as needed. Cyclic voltammetry (CV) was performed (20 $mV \cdot s^{-1}$) on a potentiostat (CH instruments 604e) in acetonitrile with lithium perchlorate (0.1 M) in a three-electrode configuration (working, FTO/NiO/treatment; counter, platinum mesh; reference, Ag/AgCl). Density of states (DOS) was calculated from the cathodic wave of the CV utilizing film thicknesses measured with profilometry and by assuming a porosity of 50%. The difference spectra of the DOS were fit to the summation of three Gaussian peaks centered at −0.11, 0.10, and 0.55 V vs Ag/AgCl.

$J-V$ curves were obtained under back-illumination using a Newport Oriel 150 W class ABB AM1.5G solar simulator calibrated to 1-sun intensity with a certified reference solar cell (Newport 91150 V) using a Keithley 2636A sourcemeter (resolution, 1 mV; measure delay, 0.1 s). Devices were tested over several days before plateauing up to a final performance. All DSSC performance metrics and $J-V$ curves reported are stabilized performance values. η, V_{OC}, J_{SC}, FF, and series resistance were extracted from the light $J-V$ curves. J_0 was extracted by fitting the dark $J-V$ curves to the ideal diode equation in the linear small forward bias region. Incident photon to current efficiency (IPCE/EQE) measurements were obtained by illuminating devices with a tungsten lamp (Newport Instruments) coupled to a spectrometer (Princeton Instruments SP-2300). Room light was excluded from the devices by enclosing the devices during testing in a black-out container. Internal quantum efficiency (IQE) measurements were obtained by normalizing the EQE spectra by the LHE. Device carrier lifetimes were obtained from V_{OC} decays

DOI: 10.1021/acs.jpcc.6b06593
J. Phys. Chem. C XXXX, XXX, XXX−XXX

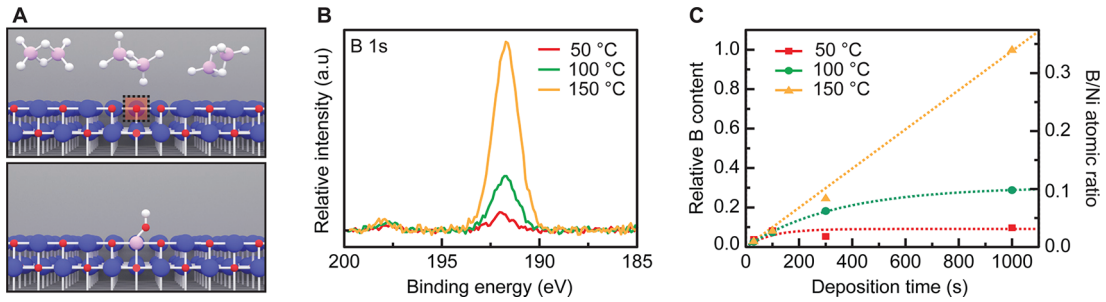

Figure 1. TAD of B on nanoparticle NiO. (A) Schematic illustration of the TAD process, showing introduction of diborane with site-selective deposition at a Ni vacancy denoted by the dashed box (top) and conversion to boron hydroxide after exposure to air (bottom). (B) XPS spectra of the B 1s peak for NiO samples treated with B_2H_6 for 1000 s at temperatures of 50 °C (red), 100 °C (green), and 150 °C (yellow). Each spectrum is normalized by the integrated intensity of the Ni 2p spectra collected on the same sample to reflect the relative B to Ni atomic ratio in the surface region probed by XPS [see Figure S1 of the Supporting Information (SI) for additional details]. (C) Relative B content as a function of deposition time at 50 °C (red squares), 100 °C (green circles), and 150 °C (yellow triangles). Red and green dashed lines represent a fit to a monoexponential rise for 50 and 100 °C data, respectively, and yellow dashed line represents a linear fit for 150 °C data. B-content is reported as the B to Ni atomic ratio.

(sampling rate, 1 kHz) with a starting illumination of 1-sun and a shutter response of <1 s. The decay was fit to a triexponential decay with an adjusted $R^2 > 0.98$. The time derivative of the fit was used to determine the lifetime.

Theoretical Method. The first-principles calculations here closely follow the computational details as described in ref 49. Density functional theory (DFT) calculations were performed with the Hubbard correction using the Quantum Espresso code.[50] The interaction of the valence electrons with ionic cores was described by Vanderbilt ultrasoft pseudopotentials,[51] and the Kohn−Sham wave functions were represented in a plane-wave basis set, where the energy cutoffs of the wave functions and the density were 48 and 300 Ry, respectively. The surface Brillouin zone integration was performed with a 4 × 4 × 1 Monkhorst−Pack[52] *k*-point grid. Spin-polarized calculations were carried out in this present work because of the antiferromagnetic nature of both bulk NiO and NiO(111) surfaces. In our calculation, the Hubbard *U* correction approach[53−56] was applied to the generalized-gradient approximation (GGA) of Perdew, Burke, and Ernzerhof (PBE),[57] because of the strong electron correlation of the partially filled d-shells in Ni atoms. The Hubbard parameter *U* and exchange parameter *J* are not considered separately, but they are combined as an effective parameter U_{eff} ($U_{eff} = U - J$).[58] The value of U_{eff} was set to 5.4 eV, as in previous works.[45,49,59−63] To simulate the surface structure, a 76-atom supercell (24.10 Å in thickness) was used, modeling the ideal octopolar reconstructed NiO(111) surface. In our calculations, all the surfaces are modeled by periodically repeating symmetric slabs. The vacuum region between the repeated slabs is set to 15 Å, so the interaction between repeating slabs in the vacuum direction is negligible. The octopolar reconstruction phase was considered in this present work because of its energetic stability found in other works.[62,64−69] The Ni vacancy and B-doping structure are modeled using this octopolar reconstructed structure by removing or substituting one nickel atom with a boron atom in the third layer, which is the first stoichiometric layer below the reconstructed surface.

3. RESULTS AND DISCUSSION

Characterizing the Deposition of B. The TAD process, as illustrated schematically in Figure 1A, was performed with diborane gas in a conventional CVD system to deposit B on mesoporous thin films of NiO. The relative B content was determined by X-ray photoelectron spectroscopy (XPS) for temperatures of 50, 100, and 150 °C and for deposition times between 30 and 1000 s, as exemplified by the data for 1000 s in Figure 1B. The deposition at 50 and 100 °C plateaus at sufficiently long deposition times (Figure 1C), and the kinetic traces are each well-fit to a monoexponential rise, corresponding to first-order kinetics. At 150 °C, however, a linear deposition rate is observed, indicating the presence of a homogeneous decomposition typical of a CVD process. The first-order kinetics at lower temperatures indicate that the deposition process in this regime is self-limited, and for long deposition times, the amount of B deposition at 100 °C is ∼3 times larger than at 50 °C. In addition, the observed rate constant at 50 °C is ∼4 times higher than at 100 °C. These differences in deposition rate and deposition extent suggest that there might be more than one type of reactive surface site, giving rise to different rate constants, and suggest that the 100 °C deposition is able to deposit and passivate a larger fraction of these sites.

We further examined the Ni 2p and O 1s XPS spectra to survey the chemical character of the untreated and B-treated NiO electrodes. The Ni 2p spectra of the untreated, 50, and 100 °C samples are nearly identical (Figure 2A), but the spectrum changes significantly at a deposition temperature of 150 °C. In particular, the ratio of the peaks at 853 and 855 eV invert, indicating a fundamental change in the Ni character, which reflects a change in the local electron density around Ni atoms caused by changes to the bonding environment and oxidation state of the atom. From our previous work,[45] it was observed that this inversion of the ratio was correlated with a decrease in device performance.

The O 1s spectra are shown in Figure 2B and were collected on samples exposed to ambient conditions after TAD deposition. Spectra of the B-treated films show the growth of a feature at higher binding energy, ∼532 eV, indicative of $[B(OH)_x]$-like species, which increases with deposition temperature. At a deposition temperature of 150 °C, the peak substantially increases in amplitude, and two additional peaks appear at 530.0 and 532.9 eV (see Figure S2 of the SI for fits to the spectra). The growth of these new peaks at high temperature is consistent with the formation of a boron oxide, BO_x, species as a result of homogeneous CVD of B followed by oxidation under ambient conditions. The combined XPS results in Figures 1 and 2 indicate that a conventional CVD process

DOI: 10.1021/acs.jpcc.6b06593
J. Phys. Chem. C XXXX, XXX, XXX−XXX

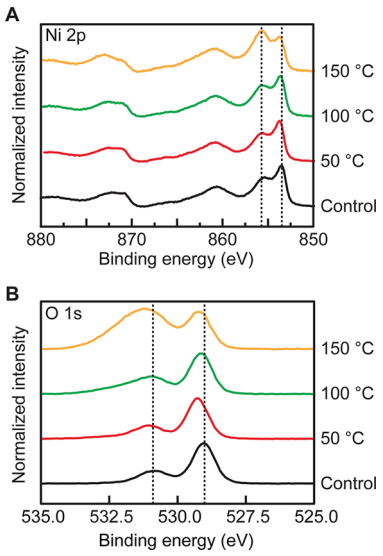

Figure 2. Chemical characterization of TAD-treated NiO by XPS. Spectra in (A) the Ni 2p region and (B) the O 1s region, showing spectra without treatment (black traces) and with TAD treatment at 50 °C (red traces), 100 °C (green traces), and 150 °C (yellow traces) for 1000 s.

occurs at 150 °C, coating the material in a film; however, a different, self-limited deposition process, which does not substantially alter the chemical bonding environment on the surface of the film, occurs at lower temperatures. These observations are consistent with the TAD deposition process.[45]

Passivation of Optical and Electronic Surface Defects. As shown in Figure 3A, the dark coloring of NiO films was bleached by the diborane treatment. The absorbance of films treated at each deposition temperature (Figure 3B) shows a bleach in the visible and near-infrared spectral regions, and

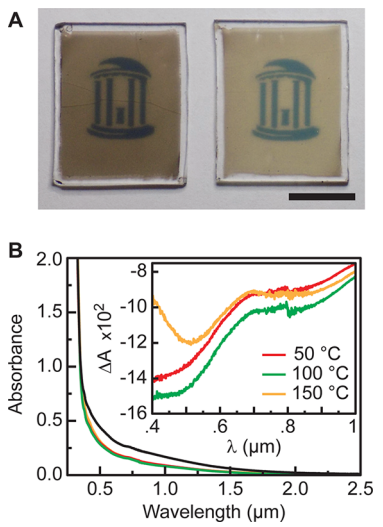

Figure 3. Optical bleaching of NiO. (A) Optical images of 1.0-μm-thick mesoporous NiO nanoparticle films on glass slides without treatment (left) and with a TAD treatment at 100 °C (right); scale bar, 1 cm. (B) Absorbance spectra of 1.0-μm-thick films for untreated NiO (black) and TAD treatment at 50 °C (red), 100 °C (green), and 150 °C (yellow). Inset: difference spectra determined by subtracting the spectra of the untreated NiO from the spectra of the TAD-treated films.

difference spectra (inset of Figure 3B) show two distinct features, including a peak at ~500 nm and a long tail into the near-infrared. The shape of the bleach matches well with the bleach obtained by a TAD of Al.[45]

The electronic properties of the NiO films were probed by cyclic voltammetry. As shown in Figure 4A, the voltammogram of the untreated film shows reversible peaks above and within the valence band of NiO at ~0.4 V vs Ag/AgCl. These peaks have been reported in the literature on NiO[70] and assigned to Ni^{2+}–Ni^{3+} proton-coupled electron transfer reactions based on pH-dependent studies. However, our recent results[45] indicate that the peaks are better assigned as oxygen-localized defect states, which are expected to exhibit a Nernstian shift of −59 mV per pH unit, as observed in previous studies,[70] because of conventional acid/base equilibria. The amplitudes in the cyclic voltammograms diminish upon diborane treatment, which is consistent with the passivation of these defect states. Because the majority of the peaks are positioned within the band gap of NiO and are removed by surface deposition of B, we assign the peaks as surface trap-state levels. Despite the substantial decrease in amplitude of the peaks upon B treatment, a reversible peak at ~0.1 V vs Ag/AgCl is still apparent in the voltammograms, even for 100 and 150 °C deposition. In comparison, all apparent reversible peaks were removed in voltammograms collected after TAD of Al[45] (Figure S3, SI), suggesting that passivation with B is not as complete as passivation with Al.

The DOS as a function of applied potential was calculated from the cathodic wave of the voltammograms, as shown in Figure 4B. For 1000 s of treatment, the integrated DOS, from −0.5 to 1.0 V vs Ag/AgCl, decreases by ~34% at 50 °C treatment and by ~53% at both 100 and 150 °C. Thus, TAD of B passivates a large portion of the defect states, but the passivation is not complete. The optical bleaching of the films (cf. Figure 3) can be explained by the passivation of electronic states, which removes optical transitions from filled states in the valence band into the trap-state levels. However, the bleaching is less pronounced compared to our previous report of Al,[45] because of the incomplete electronic passivation.

The change in DOS (ΔDOS) upon diborane treatment was calculated by subtracting the DOS of the untreated film from the DOS of the treated films, as shown in Figure 4C. The spectra are well-fit (see Figure S4, SI) to three Gaussian functions centered at −0.11, 0.10, and 0.55 V vs Ag/AgCl, as exemplified by the dashed lines in Figure 4C for the 50 °C data. The peaks are qualitatively similar to those we previously reported for NiO ultrathin, quasi-two-dimensional nanoplatelets, which were oriented in the ⟨111⟩ crystallographic direction.[29] Here, we observe similar peak positions but a different ratio of peak intensities, which likely results from the different NiO crystal faces present in the nanoparticle sample used in the current study. Similar differences in peak intensities and total chemical capacitance were recently reported by Wood et al.[71] when comparing multiple forms of NiO. The ΔDOS spectra show that, for 1000 s of deposition, there is no appreciable difference between the passivation at 100 and 150 °C, and the passivation at 50 °C saturates at ~60% of the passivation at 100 or 150 °C. In addition, we probed the dependence of ΔDOS on deposition time at 100 °C (Figure S5, SI), which indicated that substantial electronic passivation occurs between 300 and 1000 s, even though less B is deposited with the longer time scales. The results on the optical and electronic passivation of NiO indicate that the B deposition

DOI: 10.1021/acs.jpcc.6b06593
J. Phys. Chem. C XXXX, XXX, XXX−XXX

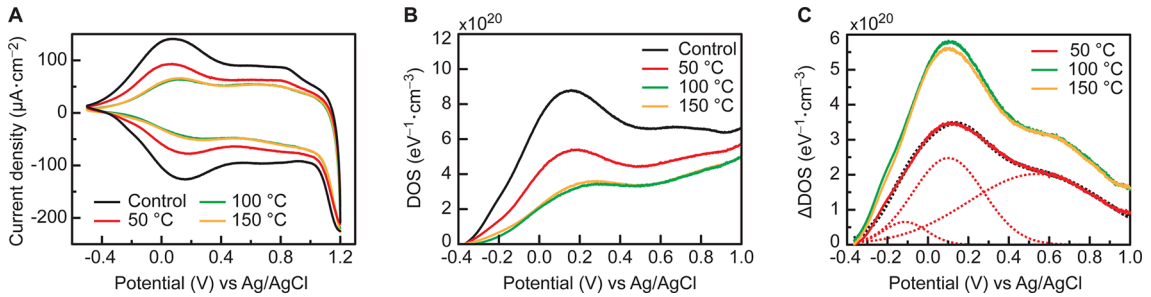

Figure 4. Electronic bleaching of NiO after 1000 s of TAD treatment. (A) Cyclic voltammograms versus Ag/AgCl potential for untreated films (black) and TAD-treated films deposited at 50 °C (red), 100 °C (green), and 150 °C (yellow). (B) DOS versus Ag/AgCl for untreated films (black) and TAD-treated films deposited at 50 °C (red), 100 °C (green), and 150 °C (yellow). (C) Change in DOS (solid lines) as a function of applied potential for TAD-treated films at 50 °C (red), 100 °C (green), and 150 °C (yellow). Dashed red lines represent a fit of the 50 °C spectrum to three Gaussian functions, and the black dashed line represents the summation of the Gaussian functions.

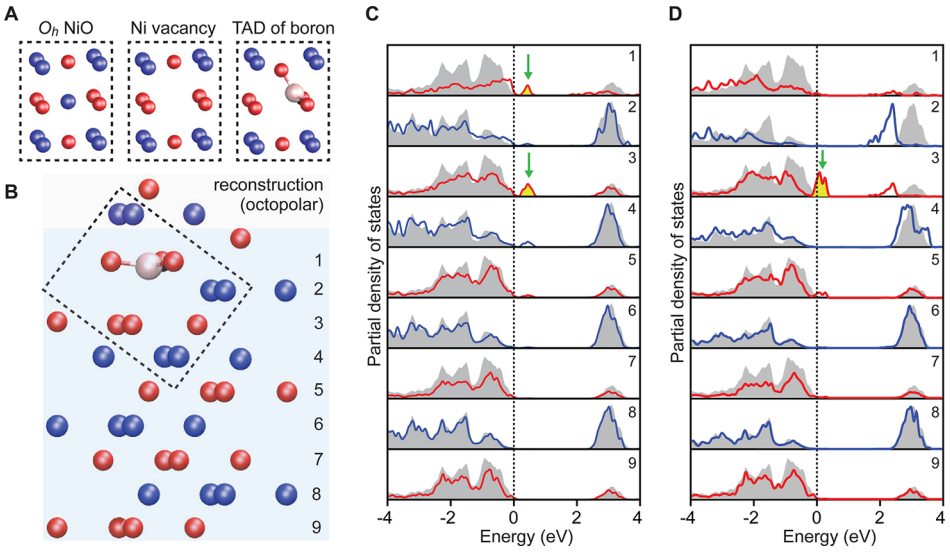

Figure 5. First-principles calculations of B passivation. (A) Structure of the passivated Ni vacancy, showing stoichiometric NiO with octahedrally coordinated Ni (left), the Ni vacancy (middle), and the B-passivated vacancy (right). Ni, O, and B atoms are depicted as blue, red, and pink, respectively. (B) Structure of the NiO(111) surface with a single Ni vacancy passivated with B. The image depicts the simulation supercell used for calculations with periodic boundary conditions in the surface lateral direction. The numbers on the right represent the stoichiometric atomic layers below the octopolar surface reconstruction. The dashed box corresponds to the right-hand image of panel A. (C) Layer-dependent density of states (DOS) calculated for a Ni vacancy in layer 2, with the red and blue curves corresponding to oxygen and nickel layers, respectively. The dashed line represents the valence band maximum of NiO. The DOS for bulk NiO is shown by the gray shaded area. The Ni vacancy induces trap states within the energy gap, as denoted by the green arrows and yellow-shaded area. Image reproduced with permission from ref 45. (Copyright 2016 American Chemical Society.) (D) Layer-dependent DOS for the B-passivated NiO surface corresponding to the structure shown in panel B. Red and blue curves correspond to oxygen and nickel layers, respectively, and the dashed line represents the valence band maximum of NiO. The DOS for bulk NiO is shown by the gray shaded area. The remaining trap states after B passivation are denoted by the green arrow and yellow-shaded areas.

directly passivates the trap states in the material, which is consistent with the mechanism of TAD.

First-Principles Calculation of B Passivation. To understand the origin of B passivation of NiO vacancy defects, the (111) surface of NiO was modeled using density functional theory with the Hubbard correction, which was necessary to account for the strong electron correlation from the partially filled Ni 3d orbitals.[63] Previously, Ni vacancy defects were shown to create localized trap-state densities originating on O atoms near the vacancy.[45] These trap states matched well with experimental measurements, confirming the existence of states slightly above the valence band edge associated with Ni vacancies.

The passivation of the Ni vacancy with B was explored by substituting a Ni atom in the first stoichiometric layer with a B atom, as shown in Figure 5A. By performing a geometry optimization, we found that the boron atom preferentially positions itself in a face of the octahedron (rather than the octahedral lattice position of the missing Ni atom), as shown in Figure 5A,B. The bonding interaction with only three O atoms of the six in the octrahedral (O_h) symmetry of the local bonding indicates that only partial passivation of the unsaturated bonding is possible with a single boron, unlike our previous observation for an Al atom.[45]

To further examine the partial passivation, layer-dependent DOS calculations were performed. The surface with a Ni vacancy in the lattice shows the formation of trap states above the valence band edge (Figure 5C). As is shown in Figure 5D, the presence of a B atom was found to remove the trap-state density in layer 1, where the B atom is directly bonded to three O atoms adjacent to the vacancy. However, trap-state density still remains in layer 3, which contains the other three

DOI: 10.1021/acs.jpcc.6b06593
J. Phys. Chem. C XXXX, XXX, XXX−XXX

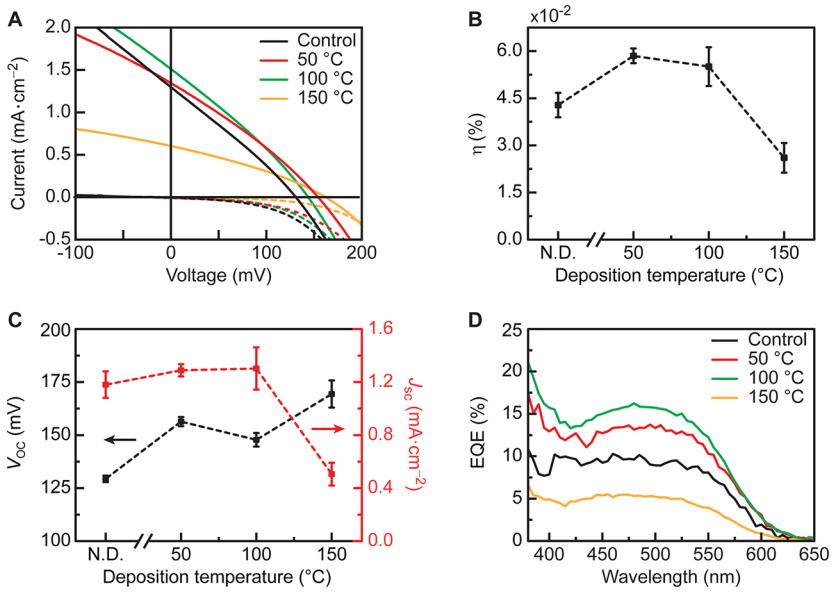

Figure 6. p-Type dye-sensitized solar cell device performance. (A) Champion $J-V$ curves under simulated 1-sun illumination (solid lines) and in the dark (dashed lines) for NiO devices sensitized with the P1 chromophore in a standard I^-/I_3^- electrolyte without treatment (black trace) and with a TAD of B for 1000 s at 50 °C (red trace), 100 °C (green trace), and 150 °C (yellow trace). (B) Average power-conversion efficiencies, η, under 1-sun illumination as a function of deposition temperature. (C) V_{OC} (black trace and left-hand axis) and J_{SC} (red trace and right-hand axis) as a function of deposition temperature. (D) EQE spectra of champion NiO devices without treatment (black) and with a TAD of B at 50 °C (red), 100 °C (green), and 150 °C (yellow) for 1000 s. Average values and standard deviations, represented by error bars, are calculated from a sample size of four. N.D. refers to no deposition and represents the untreated NiO sample.

Table 1. Average[a] Photovoltaic Characteristics for NiO DSSC Devices Treated with TAD of B at Various Temperatures and 1000 s of Deposition

deposition T (°C)	J_{SC} (mA·cm^{-2})	V_{OC} (mV)	FF (%)	η (%)	J_0 (A·cm^{-2})	R_S (Ω·cm^2)
N.D.[b]	1.2 ± 0.1	129 ± 1	28.0 ± 0.3	0.043 ± 0.004	(9 ± 2) × 10^{-6}	77 ± 6
50	1.29 ± 0.05	156 ± 2	29.0 ± 0.3	0.058 ± 0.002	(6 ± 3) × 10^{-6}	81 ± 3
100	1.3 ± 0.2	148 ± 3	28.6 ± 0.3	0.055 ± 0.006	(5.4 ± 0.9) × 10^{-6}	77 ± 6
150	0.51 ± 0.09	169 ± 6	30.4 ± 0.8	0.026 ± 0.005	(2.5 ± 0.7) × 10^{-6}	200 ± 40

[a]Averages and standard deviations reflect a sample size of 4. [b]N.D. refers to no deposition and represents the untreated NiO sample.

Table 2. Champion[a] Photovoltaic Characteristics for NiO DSSC Devices Treated with TAD of B at Various Temperatures and 1000 s of Deposition

deposition T (°C)	J_{SC} (mA·cm^{-2})	V_{OC} (mV)	FF (%)	η (%)	J_0 (A·cm^{-2})	R_S (Ω·cm^2)
N.D.[b]	1.30	131	27.7	0.047	1.01 × 10^{-5}	72.5
50	1.34	154	29.2	0.061	1.06 × 10^{-5}	77.2
100	1.51	144	28.8	0.063	6.63 × 10^{-6}	64.8
150	0.60	162	31.4	0.031	3.38 × 10^{-6}	149.6

[a]Champion devices were identified by the highest photoconversion efficiency, η. [b]N.D. refers to no deposition and represents the untreated NiO sample.

remaining O atoms adjacent to the Ni vacancy that are not bonded to the B atom. This first-principles result is in good agreement with the experimental measurements, which show that only partial optical and electronic passivation is possible with the diborane treatment when compared to the passivation observed previously with Al.[45]

Performance of p-Type DSSCs. We fabricated a series of p-type DSSC devices to determine the effect of the TAD of B on the photovoltaic performance of NiO. We utilized a commercially available and well-studied hole-injecting chromophore, P1,[17,23−28] and a standard I^-/I_3^- electrolyte. Current density vs voltage ($J-V$) curves were collected in the dark and under simulated 1-sun illumination, as shown in Figure 6A, and the average and champion photovoltaic device metrics are summarized in Tables 1 and 2, respectively. Photovoltaic performance for the devices without TAD treatment are consistent with literature reports,[17,23,25−28,45] producing photoconversion efficiencies (η) of 0.043 ± 0.004%. Upon 50 °C treatment with a TAD of B, η increases by 35% to 0.058 ± 0.002%, as shown in Figure 6B. Similarly, the treatment at 100 °C increases η to 0.055 ± 0.006%, but η decreases at a deposition temperature of 150 °C. As shown in Figure 6C, the decrease in η is due to a sharp decrease in the short-circuit current density (J_{SC}) at 150 °C. The decrease in J_{SC} is correlated with an increase in the series resistance (R_S) from 77 ± 6 Ω·cm^2 for untreated NiO to 200 ± 40 Ω·cm^2 for 150 °C TAD-treated NiO. The increase in R_S is likely to be the result of

DOI: 10.1021/acs.jpcc.6b06593
J. Phys. Chem. C XXXX, XXX, XXX−XXX

insulating boron oxide species from homogeneous CVD deposition on the material surface.

Figure 6C also displays the open-circuit voltage (V_{OC}) as a function deposition temperature, which shows an increase from 129 ± 1 mV for the untreated film to 156 ± 2 mV at 50 °C deposition. Upon CVD of boron oxide at 150 °C, the V_{OC} rises to 169 ± 6 mV. The increases in V_{OC} are well-correlated with a decrease in J_0 by nearly 3-fold. However, the improvement in V_{OC} and J_0 is substantially less than the improvement observed from TAD of Al.[45] This difference likely results from the incomplete passivation of the electronic defect states with B (cf. Figures 4 and 5). The device charge carrier lifetimes were obtained by measuring the V_{OC} decay with a starting illumination of 1 sun (Figure S6, SI). The TAD of B treatment increases the lifetime by ∼2-fold at a given V_{OC}. However, similar to the V_{OC}, the increase in lifetime is substantially less than the improvement observed with TAD of Al.[45]

The J_{SC} values of devices treated at 50 and 100 °C are equivalent to or slightly higher than the values measured from the untreated devices. Unlike the prior results on TAD of Al, we do not observe a decrease in J_{SC} as a result of the TAD of B.[45] External quantum efficiency (EQE) measurements on the champion devices are shown in Figure 6D. The spectral shape of each trace matches well with the light-harvesting efficiencies (LHEs) (Figure S7, SI) of the P1 chromophore bound to the surface of NiO. The internal quantum efficiencies of the devices were also calculated (Figure S7 and Table S1, SI) and show, on average, a 15−20% improvement at 50 and 100 °C treatments. The results suggest that the TAD treatment modestly increases the efficiency of charge separation and collection in the devices, an effect that will be investigated in future time-resolved studies.

Although the results on both TAD of B and TAD of Al show that the V_{OC} is substantially improved because of a reduction in recombination rates, causing a lower J_0, it is interesting to note that the fill factor of the devices is not improved. This result suggests that the trap states associated with Ni vacancies cause the recombination (measured in the dark $J-V$ curve) that lowers V_{OC} but do not cause the recombination that lowers the fill factor. As discussed by Wu et al.,[39] there are two potential recombination processes in NiO DSSC devices. The first is between the semiconductor and the electrolyte and the second is between the semiconductor and the reduced chromophore. The TAD passivation results suggest that the Ni vacancy trap states are the primary contributor to the first recombination process, which occurs in the dark and in the light, but do not participate in the second recombination process, which occurs only in the light. The origin of the low fill factor, which can most likely be attributed to recombination between the semiconductor and reduced chromophore, is still an open question, although the low dielectric constant of NiO may play an important role in facilitating this recombination process.

4. CONCLUSION

We have shown that TAD of B can successfully passivate surface trap states of the widely used photocathode material NiO. The deposition rates were shown to obey first-order rate kinetics up to 100 °C, after which zeroth-order rate behavior was observed, resulting in homogeneous CVD on the electrode. Optical and electronic bleaching of the NiO electrodes were observed, indicating the successful passivation of surface trap states near the valence band. First-principles calculations indicate that boron is able to passivate up to three O atoms within an octahedral defect site containing six O atoms. Thus, a single boron atom is unable to completely passivate a single Ni vacancy, and trap states remain above the valence band edge. p-Type DSSCs showed a modest improvement in the V_{OC}, indicating that the partial passivation of the trap state with TAD of B does improve the photovoltaic performance. However, the improvement is less dramatic than previously achieved with TAD of Al by a modified ALD process.[45] The results presented here indicate that the TAD process can be used with a variety of vapor-phase precursors and highlight the need to carefully choose both the deposition conditions and chemical identity of the precursor to achieve successful, site-selective passivation of defect sites in nanomaterials.

■ ASSOCIATED CONTENT

Supporting Information

The Supporting Information is available free of charge on the ACS Publications website at DOI: 10.1021/acs.jpcc.6b06593.

Figures S1−S7 and Table S1 (PDF)

■ AUTHOR INFORMATION

Corresponding Author

*E-mail: jfcahoon@unc.edu.

Author Contributions

C.J.F. and J.F.C. conceived and designed the experiments and wrote the manuscript. S.M.M. assisted with experimental measurements. C.L.D. performed XPS measurements and interpretation. L.L and Y.K. performed first-principles calculations. All authors commented on the manuscript and assisted in the analysis and interpretation of the data.

Notes

The authors declare no competing financial interest.

■ ACKNOWLEDGMENTS

This work was primarily funded by the UNC Energy Frontier Research Center (EFRC) "Center for Solar Fuels", an EFRC funded by the U.S. Department of Energy, Office of Science, Office of Basic Energy Sciences, under Award DE-SC0001011. S.M.M. acknowledges a National Science Foundation (NSF) individual graduate research fellowship. We acknowledge T. Celano for 3D graphics. This work made use of instrumentation at the Chapel Hill Analytical and Nanofabrication Laboratory (CHANL), a member of the North Carolina Research Triangle Nanotechnology Network (RTNN), which is supported by the NSF (grant ECCS-1542015) as part of the National Nanotechnology Coordinated Infrastructure (NNCI).

■ REFERENCES

(1) Peters, G. P.; Andrew, R. M.; Boden, T.; Canadell, J. G.; Ciais, P.; Le Quere, C.; Marland, G.; Raupach, M. R.; Wilson, C. The Challenge to Keep Global Warming Below 2 °C. *Nat. Clim. Change* **2013**, *3*, 4−6.

(2) Parida, B.; Iniyan, S.; Goic, R. A Review of Solar Photovoltaic Technologies. *Renewable Sustainable Energy Rev.* **2011**, *15*, 1625−1636.

(3) Concepcion, J. J.; House, R. L.; Papanikolas, J. M.; Meyer, T. J. Chemical Approaches to Artificial Photosynthesis. *Proc. Natl. Acad. Sci. U. S. A.* **2012**, *109*, 15560−15564.

(4) Alibabaei, L.; Luo, H.; House, R. L.; Hoertz, P. G.; Lopez, R.; Meyer, T. J. Applications of metal oxide materials in dye sensitized photoelectrosynthesis cells for making solar fuels: let the molecules do the work. *J. Mater. Chem. A* **2013**, *1*, 4133−4145.

(5) Alibabaei, L.; Sherman, B. D.; Norris, M. R.; Brennaman, M. K.; Meyer, T. J. Visible Photoelectrochemical Water Splitting into H_2 and

DOI: 10.1021/acs.jpcc.6b06593
J. Phys. Chem. C XXXX, XXX, XXX−XXX

O_2 in a Dye-Sensitized Photoelectrosynthesis Cell. *Proc. Natl. Acad. Sci. U. S. A.* **2015**, *112*, 5899−5902.
(6) Song, W.; Chen, Z.; Glasson, C. R. K.; Hanson, K.; Luo, H.; Norris, M. R.; Ashford, D. L.; Concepcion, J. J.; Brennaman, M. K.; Meyer, T. J. Interfacial Dynamics and Solar Fuel Formation in Dye-Sensitized Photoelectrosynthesis Cells. *ChemPhysChem* **2012**, *13*, 2882−2890.
(7) Song, W.; Brennaman, M. K.; Concepcion, J. J.; Jurss, J. W.; Hoertz, P. G.; Luo, H.; Chen, C.; Hanson, K.; Meyer, T. J. Interfacial Electron Transfer Dynamics for $[Ru(bpy)_2((4,4'\text{-}PO_3H_2)_2bpy)]_2$+ Sensitized TiO_2 in a Dye-Sensitized Photoelectrosynthesis Cell: Factors Influencing Efficiency and Dynamics. *J. Phys. Chem. C* **2011**, *115*, 7081−7091.
(8) Song, W.; Glasson, C. R. K.; Luo, H.; Hanson, K.; Brennaman, M. K.; Concepcion, J. J.; Meyer, T. J. Photoinduced Stepwise Oxidative Activation of a Chromophore−Catalyst Assembly on TiO_2. *J. Phys. Chem. Lett.* **2011**, *2*, 1808−1813.
(9) Song, W.; Luo, H.; Hanson, K.; Concepcion, J. J.; Brennaman, M. K.; Meyer, T. J. Visualization of Cation Diffusion at the TiO_2 Interface in Dye Sensitized Photoelectrosynthesis Cells (DSPEC). *Energy Environ. Sci.* **2013**, *6*, 1240−1248.
(10) Vos, A. D. Detailed Balance Limit of the Efficiency of Tandem Solar Cells. *J. Phys. D: Appl. Phys.* **1980**, *13*, 839.
(11) Hu, S.; Xiang, C.; Haussener, S.; Berger, A. D.; Lewis, N. S. An Analysis of the Optimal Band Gaps of Light Absorbers in Integrated Tandem Photoelectrochemical Water-Splitting Systems. *Energy Environ. Sci.* **2013**, *6*, 2984−2993.
(12) Nozik, A. J. PN Photoelectrolysis Cells. *Appl. Phys. Lett.* **1976**, *29*, 150−153.
(13) Knauf, R. R.; Kalanyan, B.; Parsons, G. N.; Dempsey, J. L. Charge Recombination Dynamics in Sensitized SnO_2/TiO_2 Core/Shell Photoanodes. *J. Phys. Chem. C* **2015**, *119*, 28353−28360.
(14) Lapides, A. M.; Sherman, B. D.; Brennaman, M. K.; Dares, C. J.; Skinner, K. R.; Templeton, J. L.; Meyer, T. J. Synthesis, Characterization, and Water Oxidation by a Molecular Chromophore-Catalyst Assembly Prepared by Atomic Layer Deposition. The "Mummy" Strategy. *Chemical Science* **2015**, *6*, 6398−6406.
(15) Wu, F.; Liu, J.; Li, X.; Song, Q.; Wang, M.; Zhong, C.; Zhu, L. D−A−A-Type Organic Dyes for NiO-Based Dye-Sensitized Solar Cells. *Eur. J. Org. Chem.* **2015**, *2015*, 6850−6857.
(16) Sheibani, E.; Zhang, L.; Liu, P.; Xu, B.; Mijangos, E.; Boschloo, G.; Hagfeldt, A.; Hammarstrom, L.; Kloo, L.; Tian, H. A Study of Oligothiophene-Acceptor Dyes in p-Type Dye-Sensitized Solar Cells. *RSC Adv.* **2016**, *6*, 18165−18177.
(17) Qin, P.; Zhu, H.; Edvinsson, T.; Boschloo, G.; Hagfeldt, A.; Sun, L. Design of an Organic Chromophore for p-Type Dye-Sensitized Solar Cells. *J. Am. Chem. Soc.* **2008**, *130*, 8570−8571.
(18) Nattestad, A.; Mozer, A. J.; Fischer, M. K. R.; Cheng, Y. B.; Mishra, A.; Bauerle, P.; Bach, U. Highly efficient photocathodes for dye-sensitized tandem solar cells. *Nat. Mater.* **2010**, *9*, 31−35.
(19) Click, K. A.; Beauchamp, D. R.; Huang, Z.; Chen, W.; Wu, Y. Membrane-Inspired Acidically Stable Dye-Sensitized Photocathode for Solar Fuel Production. *J. Am. Chem. Soc.* **2016**, *138*, 1174−1179.
(20) Click, K. A.; Beauchamp, D. R.; Garrett, B. R.; Huang, Z.; Hadad, C. M.; Wu, Y. A Double-Acceptor as a Superior Organic Dye Design for p-type DSSCs: High Photocurrents and the Observed Light Soaking Effect. *Phys. Chem. Chem. Phys.* **2014**, *16*, 26103−26111.
(21) Perera, I. R.; Daeneke, T.; Makuta, S.; Yu, Z.; Tachibana, Y.; Mishra, A.; Bäuerle, P.; Ohlin, C. A.; Bach, U.; Spiccia, L. Application of the Tris(acetylacetonato)iron(III)/(II) Redox Couple in p-Type Dye-Sensitized Solar Cells. *Angew. Chem., Int. Ed.* **2015**, *54*, 3758−3762.
(22) Zhang, X. L.; Zhang, Z.; Chen, D.; Bauerle, P.; Bach, U.; Cheng, Y.-B. Sensitization of nickel oxide: improved carrier lifetime and charge collection by tuning nanoscale crystallinity. *Chem. Commun.* **2012**, *48*, 9885−9887.
(23) Gibson, E. A.; Awais, M.; Dini, D.; Dowling, D. P.; Pryce, M. T.; Vos, J. G.; Boschloo, G.; Hagfeldt, A. Dye sensitised solar cells with nickel oxide photocathodes prepared via scalable microwave sintering. *Phys. Chem. Chem. Phys.* **2013**, *15*, 2411−2420.
(24) Zannotti, M.; Wood, C. J.; Summers, G. H.; Stevens, L. A.; Hall, M. R.; Snape, C. E.; Giovanetti, R.; Gibson, E. A. Ni Mg Mixed Metal Oxides for p-Type Dye-Sensitized Solar Cells. *ACS Appl. Mater. Interfaces* **2015**, *7*, 24556−24565.
(25) Li, L.; Gibson, E. A.; Qin, P.; Boschloo, G.; Gorlov, M.; Hagfeldt, A.; Sun, L. Double-Layered NiO Photocathodes for p-Type DSSCs with Record IPCE. *Adv. Mater.* **2010**, *22*, 1759−1762.
(26) Huang, Z.; Natu, G.; Ji, Z.; Hasin, P.; Wu, Y. P-Type Dye-Sensitized NiO Solar Cells: A Study by Electrochemical Impedance Spectroscopy. *J. Phys. Chem. C* **2011**, *115*, 25109−25114.
(27) Natu, G.; Huang, Z.; Ji, Z.; Wu, Y. The Effect of an Atomically Deposited Layer of Alumina on NiO in p-type Dye-Sensitized Solar Cells. *Langmuir* **2012**, *28*, 950−956.
(28) Qin, P.; Linder, M.; Brinck, T.; Boschloo, G.; Hagfeldt, A.; Sun, L. High Incident Photon-to-Current Conversion Efficiency of p-Type Dye-Sensitized Solar Cells Based on NiO and Organic Chromophores. *Adv. Mater.* **2009**, *21*, 2993−2996.
(29) Flynn, C. J.; Oh, E. E.; McCullough, S. M.; Call, R. W.; Donley, C. L.; Lopez, R.; Cahoon, J. F. Hierarchically-Structured NiO Nanoplatelets as Mesoscale p-Type Photocathodes for Dye-Sensitized Solar Cells. *J. Phys. Chem. C* **2014**, *118*, 14177−14184.
(30) Mercado, C. C.; Zakutayev, A.; Zhu, K.; Flynn, C. J.; Cahoon, J. F.; Nozik, A. J. Sensitized Zinc−Cobalt−Oxide Spinel p-Type Photoelectrode. *J. Phys. Chem. C* **2014**, *118*, 25340−25349.
(31) McCullough, S. M.; Flynn, C. J.; Mercado, C. C.; Nozik, A. J.; Cahoon, J. F. Compositionally-tunable mechanochemical synthesis of ZnxCo3-xO4 nanoparticles for mesoporous p-type photocathodes. *J. Mater. Chem. A* **2015**, *3*, 21990−21994.
(32) Langmar, O.; Ganivet, C. R.; Lennert, A.; Costa, R. D.; de la Torre, G.; Torres, T.; Guldi, D. M. Combining Electron-Accepting Phthalocyanines and Nanorod-like CuO Electrodes for p-Type Dye-Sensitized Solar Cells. *Angew. Chem.* **2015**, *127*, 7798−7802.
(33) Nattestad, A.; Zhang, X.; Bach, U.; Cheng, Y.-B. Dye-Sensitized $CuAlO_2$ Photocathodes for Tandem Solar Cell Applications. *J. Photonics Energy* **2011**, *1*, 011103.
(34) Yu, M.; Natu, G.; Ji, Z.; Wu, Y. P-Type Dye-Sensitized Solar Cells Based on Delafossite $CuGaO_2$ Nanoplates with Saturation Photovoltages Exceeding 460 mV. *J. Phys. Chem. Lett.* **2012**, *3*, 1074−1078.
(35) Xu, X.; Zhang, B.; Cui, J.; Xiong, D.; Shen, Y.; Chen, W.; Sun, L.; Cheng, Y.; Wang, M. Efficient p-Type Dye-Sensitized Solar Cells Based on Disulfide/Thiolate Electrolytes. *Nanoscale* **2013**, *5*, 7963−7969.
(36) Yu, M.; Draskovic, T. I.; Wu, Y. Cu(I)-Based Delafossite Compounds as Photocathodes in p-Type Dye-Sensitized Solar Cells. *Phys. Chem. Chem. Phys.* **2014**, *16*, 5026−5033.
(37) Jiang, T.; Bujoli-Doeuff, M.; Farre, Y.; Blart, E.; Pellegrin, Y.; Gautron, E.; Boujtita, M.; Cario, L.; Odobel, F.; Jobic, S. Copper Borate as a Photocathode in p-Type Dye-Sensitized Solar Cells. *RSC Adv.* **2016**, *6*, 1549−1553.
(38) Luz, A.; Conradt, J.; Wolff, M.; Kalt, H.; Feldmann, C. P-DSSCs with BiOCl and BiOBr Semiconductor and Polybromide Electrolyte. *Solid State Sci.* **2013**, *19*, 172−177.
(39) Huang, Z.; Natu, G.; Ji, Z.; He, M.; Yu, M.; Wu, Y. Probing the Low Fill Factor of NiO p-Type Dye-Sensitized Solar Cells. *J. Phys. Chem. C* **2012**, *116*, 26239−26246.
(40) Odobel, F.; Pellegrin, Y.; Gibson, E. A.; Hagfeldt, A.; Smeigh, A. L.; Hammarström, L. Recent Advances and Future Directions to Optimize the Performances of p-Type Dye-Sensitized Solar Cells. *Coord. Chem. Rev.* **2012**, *256*, 2414−2423.
(41) Natu, G.; Hasin, P.; Huang, Z.; Ji, Z.; He, M.; Wu, Y. Valence Band-Edge Engineering of Nickel Oxide Nanoparticles via Cobalt Doping for Application in p-Type Dye-Sensitized Solar Cells. *ACS Appl. Mater. Interfaces* **2012**, *4*, 5922−5929.
(42) D'Amario, L.; Boschloo, G.; Hagfeldt, A.; Hammarström, L. Tuning of Conductivity and Density of States of NiO Mesoporous

DOI: 10.1021/acs.jpcc.6b06593
J. Phys. Chem. C XXXX, XXX, XXX−XXX

Films Used in p-Type DSSCs. *J. Phys. Chem. C* **2014**, *118*, 19556−19564.
(43) Uehara, S.; Sumikura, S.; Suzuki, E.; Mori, S. Retardation of Electron Injection at NiO/Dye/Electrolyte Interface by Aluminium Alkoxide Treatment. *Energy Environ. Sci.* **2010**, *3*, 641−644.
(44) Zhang, X. L.; Huang, F.; Nattestad, A.; Wang, K.; Fu, D.; Mishra, A.; Bauerle, P.; Bach, U.; Cheng, Y.-B. Enhanced Open-Circuit Voltage of p-Type DSC with Highly Crystalline NiO Nanoparticles. *Chem. Commun.* **2011**, *47*, 4808−4810.
(45) Flynn, C. J.; McCullough, S. M.; Oh, E.; Li, L.; Mercado, C. C.; Farnum, B. H.; Li, W.; Donley, C. L.; You, W.; Nozik, A. J.; McBride, J. R.; Meyer, T. J.; Kanai, Y.; Cahoon, J. F. Site-Selective Passivation of Defects in NiO Solar Photocathodes by Targeted Atomic Deposition. *ACS Appl. Mater. Interfaces* **2016**, *8*, 4754−4761.
(46) Monk, P.; Mortimer, R.; Rosseinsky, D. *Electrochromism and Electrochromic Devices*; Cambridge University Press: Cambridge, 2007.
(47) Ito, S.; Murakami, T. N.; Comte, P.; Liska, P.; Grätzel, C.; Nazeeruddin, M. K.; Grätzel, M. Fabrication of Thin Film Dye Sensitized Solar Cells with Solar to Electric Power Conversion Efficiency over 10%. *Thin Solid Films* **2008**, *516*, 4613−4619.
(48) Christesen, J. D.; Pinion, C. W.; Grumstrup, E. M.; Papanikolas, J. M.; Cahoon, J. F. Synthetically Encoding 10 nm Morphology in Silicon Nanowires. *Nano Lett.* **2013**, *13*, 6281−6286.
(49) Ebensperger, C.; Meyer, B. First-Principles Study of the Reconstruction and Hydroxylation of the Polar NiO(111) Surface. *Phys. Status Solidi B* **2011**, *248*, 2229−2241.
(50) Giannozzi, P.; Baroni, S.; Bonini, N.; Calandra, M.; Car, R.; Cavazzoni, C.; Ceresoli, D.; Chiarotti, G. L.; Cococcioni, M.; Dabo, I.; Dal Corso, A.; de Gironcoli, S; Fabris, S.; Fratesi, G.; Gebauer, R.; Gerstmann, U.; Gougoussis, C.; Kokalj, A.; Lazzeri, M.; Martin-Samos, L.; Marzari, N.; Mauri, F.; Mazzarello, R.; Paolini, S.; Pasquarello, A.; Paulatto, L.; Sbraccia, C.; Scandolo, S.; Sclauzero, G.; Seitsonen, A. P.; Smogunov, A.; Umari, P.; Wentzcovitch, R. M. QUANTUM ESPRESSO: A Modular and Open-Source Software Project for Quantum Simulations of Materials. *J. Phys.: Condens. Matter* **2009**, *21*, 395502.
(51) Vanderbilt, D. Soft Self-Consistent Pseudopotentials in a Generalized Eigenvalue Formalism. *Phys. Rev. B: Condens. Matter Mater. Phys.* **1990**, *41*, 7892−7895.
(52) Monkhorst, H. J.; Pack, J. D. Special Points for Brillouin-Zone Integrations. *Phys. Rev. B* **1976**, *13*, 5188−5192.
(53) Anisimov, V. I.; Zaanen, J.; Andersen, O. K. Band Theory and Mott Insulators: Hubbard U instead of Stoner I. *Phys. Rev. B: Condens. Matter Mater. Phys.* **1991**, *44*, 943−954.
(54) Anisimov, V. I.; Solovyev, I. V.; Korotin, M. A.; Czyżyk, M. T.; Sawatzky, G. A. Density-Functional Theory and NiO Photoemission Spectra. *Phys. Rev. B: Condens. Matter Mater. Phys.* **1993**, *48*, 16929−16934.
(55) Liechtenstein, A. I.; Anisimov, V. I.; Zaanen, J. Density-Functional Theory and Strong Interactions: Orbital Ordering in Mott-Hubbard Insulators. *Phys. Rev. B: Condens. Matter Mater. Phys.* **1995**, *52*, R5467−R5470.
(56) Cococcioni, M.; de Gironcoli, S. Linear Response Approach to the calculation of the Effective Interaction Parameters in the LDA+U Method. *Phys. Rev. B: Condens. Matter Mater. Phys.* **2005**, *71*, 035105.
(57) Perdew, J. P.; Burke, K.; Ernzerhof, M. Generalized Gradient Approximation Made Simple. *Phys. Rev. Lett.* **1996**, *77*, 3865−3868.
(58) Dudarev, S. L.; Botton, G. A.; Savrasov, S. Y.; Humphreys, C. J.; Sutton, A. P. Electron-Energy-Loss Spectra and the Structural Stability of Nickel Oxide: An LSDA+U Study. *Phys. Rev. B: Condens. Matter Mater. Phys.* **1998**, *57*, 1505−1509.
(59) Bengone, O.; Alouani, M.; Blöchl, P.; Hugel, J. Implementation of the Projector Augmented-Wave LDA+U Method: Application to the Electronic Structure of NiO. *Phys. Rev. B: Condens. Matter Mater. Phys.* **2000**, *62*, 16392−16401.
(60) Bengone, O.; Alouani, M.; Hugel, J.; Blöchl, P. LDA+U Calculated Electronic and Structural Properties of NiO(001) and NiO(111) p(2 × 2) Surfaces. *Comput. Mater. Sci.* **2002**, *24*, 192−198.
(61) Rohrbach, A.; Hafner, J.; Kresse, G. Molecular Adsorption on the Surface of Strongly Correlated Transition-Metal Oxides: A Case Study for CO/NiO(100). *Phys. Rev. B: Condens. Matter Mater. Phys.* **2004**, *69*, 075413.
(62) Zhang, W.-B.; Tang, B.-Y. Stability of the Polar NiO(111) Surface. *J. Chem. Phys.* **2008**, *128*, 124703−124705.
(63) Li, L.; Kanai, Y. Antiferromagnetic Structures and Electronic Energy Levels at Reconstructed NiO(111) Surfaces: A DFT+U Study. *Phys. Rev. B: Condens. Matter Mater. Phys.* **2015**, *91*, 235304.
(64) Wolf, D. Reconstruction of NaCl Surfaces from a Dipolar Solution to the Madelung Problem. *Phys. Rev. Lett.* **1992**, *68*, 3315−3318.
(65) Barbier, A.; Mocuta, C.; Kuhlenbeck, H.; Peters, K. F.; Richter, B.; Renaud, G. Atomic Structure of the Polar NiO(111)- p(2 × 2) Surface. *Phys. Rev. Lett.* **2000**, *84*, 2897−2900.
(66) Erdman, N.; Warschkow, O.; Ellis, D. E.; Marks, L. D. Solution of the p(2 × 2) NiO(111) Surface Structure using Direct Methods. *Surf. Sci.* **2000**, *470*, 1−14.
(67) Subramanian, A.; Marks, L. D.; Warschkow, O.; Ellis, D. E. Direct Observation of Charge Transfer at a MgO(111) Surface. *Phys. Rev. Lett.* **2004**, *92*, 026101.
(68) Ciston, J.; Subramanian, A.; Marks, L. D. Water-Driven Structural Evolution of the Polar MgO (111) Surface: An Integrated Experimental and Theoretical Approach. *Phys. Rev. B: Condens. Matter Mater. Phys.* **2009**, *79*, 085421.
(69) Ciston, J.; Subramanian, A.; Kienzle, D. M.; Marks, L. D. Why the Case for Clean Surfaces Does Not Hold Water: Structure and Morphology of Hydroxylated Nickel Oxide (111). *Surf. Sci.* **2010**, *604*, 155−164.
(70) Boschloo, G.; Hagfeldt, A. Spectroelectrochemistry of Nanostructured NiO. *J. Phys. Chem. B* **2001**, *105*, 3039−3044.
(71) Wood, C. J.; Summers, G. H.; Clark, C. A.; Kaeffer, N.; Braeutigam, M.; Carbone, L. R.; D'Amario, L.; Fan, K.; Farre, Y.; Narbey, S.; Oswald, F.; Stevens, L. A.; Parmenter, C. D. J.; Fay, M. W.; La Torre, A.; Snape, C. E.; Dietzek, B.; Dini, D.; Hammarstrom, L.; Pellegrin, Y.; Odobel, F.; Sun, L.; Artero, V.; Gibson, E. A. A Comprehensive Comparison of Dye-Sensitized NiO photocathodes for Solar Energy Conversion. *Phys. Chem. Chem. Phys.* **2016**, *18*, 10727.

DOI: 10.1021/acs.jpcc.6b06593
J. Phys. Chem. C XXXX, XXX, XXX−XXX